Materials & Design 236 (2023) 112489

Contents lists available at ScienceDirect

Materials & Design

journal homepage: www.elsevier.com/locate/matdes

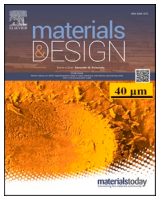

Fracture behaviour of laser powder bed fusion AlSi10Mg microlattice structures under uniaxial compression

Ninian Sing Kok Ho [a], Gin Boay Chai [a], Peifeng Li [b,*]

[a] School of Mechanical and Aerospace Engineering, Nanyang Technological University, Singapore
[b] James Watt School of Engineering, University of Glasgow, Glasgow, UK

ARTICLE INFO

Keywords:
Microlattice structures
Additive manufacturing
Powder bed fusion
Selective laser melting
Deformation
Fracture
Finite element analysis

ABSTRACT

Microlattice structures produced by laser powder bed fusion (LPBF) have been tested in compression extensively. Yet, their failure modes remain unexplained. This study bridges this research gap by accurately predicting the crack initiation process in LPBF body centred cubic (BCC) microlattices and their failure mode. In this study, LPBF AlSi10Mg BCC microlattice structures were tested in uniaxial compression and their detailed response modelled using a finite element (FE) modelling methodology on microlattices with idealised struts which was validated experimentally. Crack initiation in BCC microlattices with $2 \times 1 \times 2$ unit cells loaded in compression was observed in situ via a scanning electron microscope (SEM). The force–displacement response of the microlattice was studied with respect to crack initiation and propagation. It was found that the locations of crack initiation could be predicted by considering the equivalent plastic strain and stress triaxiality fields obtained by an FE analysis and assuming a monotonically decreasing fracture locus. Subsequently, microlattices with $4 \times 4 \times 4.5$ unit cells were similarly subjected to compression. Using a monotonically decreasing fracture locus extrapolated from uniaxial tension testing of the bulk LPBF AlSi10Mg, an FE simulation successfully predicted the commonly reported diagonal shear band failure mode of the microlattice on a model with idealised struts.

1. Introduction

Metallic microlattice structures are promising porous materials for lightweight components as well as shock absorption, heat exchange and sound absorption applications [1–6]. For a given weight, they are stronger than stochastic metallic foams due to their geometrically periodic nature [7]. Ultralight microlattice structures have been developed for future aerospace vehicles, demonstrating their potential for aerospace applications [8]. Laser powder bed fusion (LPBF) is an additive manufacturing technique suitable for metals. As expected of additive manufacturing techniques in general, LPBF can produce near net shape parts and allows for greater geometrical flexibility. As such, it has been used to manufacture microlattices of complex unit cell topologies, using various metal powders such as stainless steel, titanium alloys and aluminium alloys [9–13]. AlSi10Mg is the most commonly used alloy among the aluminium alloys that have been successfully translated to the LPBF process [14,15]. Mechanical properties of LPBF AlSi10Mg have been shown to be par with, if not superior to, those of conventionally cast AlSi10Mg alloys [16].

The mechanical properties of LPBF metallic microlattices have been widely studied, in particular their modulus and strength under quasi-static compression, i.e., their stress–strain response [3,7,9,10,17–20]. Their deformation and failure modes have also been documented extensively in the literature. While a wealth of experimental data exists in this respect, they remain purely empirical and are likely specific to the tested microlattices only as they are dependent on many factors. To fully define an LPBF microlattice, Ushijima et al. proposed that its architecture (topology), parent material, processing parameters, strut diameter, unit cell size, and unit cell shape must be specified [21]. Furthermore, experimental data obtained in past studies could not be reliably extrapolated for even microlattices of the same unit cell topology. This is because microlattices have been treated as foams in that each sample is considered as a whole without reference to how individual unit cells interact with each other. Thus, further investigation is needed to identify the underlying stress fields experienced by microlattices in compression that determine their failure modes as these have not been mapped out in detail in 3D despite their periodic geometry, even though a symmetric pattern is to be expected given the symmetries in structural geometry, loading, boundary conditions, and material properties.

Numerical modelling using the finite element (FE) method allows the

* Corresponding author.
E-mail address: peifeng.li@glasgow.ac.uk (P. Li).

https://doi.org/10.1016/j.matdes.2023.112489
Received 29 June 2023; Received in revised form 24 October 2023; Accepted 13 November 2023
Available online 14 November 2023

deformation and stress fields of arbitrary microlattice structures to be obtained and has been a typical component of investigations on the mechanical properties of microlattices. However, its application to this problem is fraught with many unknowns and limitations. Strut diameter [22], parent material properties (both elastic and plastic) [10,23], and friction coefficient [24] are parameters that have proven difficult to obtain to be input into FE simulations. In most cases, one of them is fitted such that the numerical predictions match experimental results or has its relevant parameter values assumed. In the plastic regime, Labeas and Sunaric [25] have demonstrated that FE simulations may not be able to predict localised deformations within unconstrained microlattices with vertical struts in compression (more specifically BCCZ and FCCZ microlattices), while Smith et al. [26] had to introduce imperfections into geometrical model of unconstrained BCCZ microlattices. Furthermore, among the current studies that have developed FE models of these microlattices in compression, only a few have incorporated damage models, the most common of which are based on the concept of stress triaxiality [12]. Lastly, owing to the often high computational cost of running FE simulations of microlattices, little attention has been paid to obtaining and understanding the deformation and stress fields in larger constrained microlattices.

When such microlattices are to be used in applications involving their failure, an understanding of the detailed mechanics of their failure process allows for their design such that they fail as intended. While damage models already exist in the literature [27,28], it is not clear how they fare when applied to such microlattices. This is because few studies have implemented them in FE models, and also because the initiation of damage in microlattice samples has never been observed in detail to investigate the accuracy of current damage models based on stress triaxiality, if at all. Kadkhodapour et al. [29] fitted a Johnson–Cook (J–C) fracture locus in order to match their numerical results with the experimental data. Wang and Li [12] on the other hand obtained an approximate fracture locus by considering the surface roughness of strut sized tensile specimens. Concli et al. [30] calibrated a fracture locus for 18-Ni300 and predicted the failure of single unit cell which was confirmed experimentally. However, there have not been any parametric studies on how the fracture locus affects the failure mode of microlattices.

The first aim of this study is to understand the detailed uniaxial compressive behaviour of microlattice structures using FE modelling. The issues involved with FE modelling in the process was circumvented by using ASTM E8 dogbone specimens to obtain the constitutive properties of the parent material and approximating an effective, constant (idealised) strut diameter to represent the actual specimen in the FE model. The deformation and stress fields of a microlattice with $4 \times 4 \times 4.5$ body centred cubic (BCC) unit cells can be obtained assuming that no strut failure occurs. However, past the point of strut failure in the actual compression tests, the FE model is no longer valid. In the search for information on an appropriate damage model for LPBF microlattices, additional smaller BCC microlattices comprising $2 \times 1 \times 2$ unit cells were compressed using a microtester in a scanning electron microscope (SEM) chamber and observed in-situ until strut failure occurred to search for more clues. The force–displacement response of such a microlattice in compression was studied with respect to its deformation and failure. The exact locations of the initiation sites of the first few cracks as observed were explained using its stress fields and deformation obtained by a separate FE analysis using the previously established FE methodology. Finally, the obtained clues pertaining to the fracture locus and the spatial resolution of the idealised FE model in predicting cracks were used to design a generic fracture locus for the LPBF AlSi10Mg to predict the failure mode and stress–strain response of a large microlattice with $4 \times 4 \times 4.5$ unit cells.

This study brings together the key concepts of damage modelling, the novel geometry of microlattices, and the strut imperfections caused by the LPBF process. None of these can be avoided when designing LPBF microlattice structures that are to be subjected to high strains or have to fail to serve their intended purpose. This study on how the force–displacement response, deformation, strut failure and stress fields obtained for the BCC microlattice with $4 \times 4 \times 4.5$ unit cells are related to each other at different levels can help in the design of larger components with microlattice cores.

2. Experimental procedure

2.1. Materials and specimens

Two different configurations of microlattice structures as well as solid cubes and cylinders were manufactured in an LPBF system – an SLM-250HL selective laser melting machine (SLM Solutions GmbH, Germany) using AlSi10Mg powders. Selective laser melting is an additive manufacturing technique based on the LPBF process, in which powders are fully melted [13]. The two configurations of large and small microlattices, consisting of $4 \times 4 \times 5$ and $2 \times 2 \times 2$ BCC unit cells respectively, were printed for uniaxial compression testing in different testers (Fig. 1). Note that Fig. 1 shows the schematics of machined microlattice specimens for uniaxial compression as detailed below. The nominal strut diameter of all microlattices was $d = 330$ μm and the unit cell edge length was $L = 3.0$ mm. The solid cubes and cylinders were printed horizontally while the microlattice specimens were built along their heights (i.e., the loading direction in mechanical testing). The laser power was 350 W, the scanning speed was 1150 mm s^{-1}, the layer thickness was 50 μm, and the hatch spacing was 170 μm achieved with a "stripes" pattern. All specimens were subsequently removed from the substrate plates via electrical discharge machining (EDM) for testing. Note that all specimens were tested with no additional heat treatment. A key advantage of LPBF is its ability to fabricate parts in a single step. The conclusions drawn in this study for LPBF parts not subjected to heat treatment can provide a better understanding of such parts so as to retain the economic advantages of LPBF over conventional manufacturing.

2.2. Density, microstructure, and mechanical properties of bulk LPBF AlSi10Mg

The density of each of solid cubes was measured in a Mettler Toledo XS204 analytical balance using the Archimedes principle with ethanol as the auxiliary liquid. The average density was determined to be $\rho_s = 2660$ kg m^{-3} from the measurements on three solid cubes. Given that the theoretical density of AlSi10Mg is 2680 kg m^{-3}, the relative density of the bulk LPBF AlSi10Mg is 99.25 %. Note that a maximum relative density of 99.94 % was reported in the literature [31].

The solid cubes were mounted in resin, ground, polished, and subsequently etched in Keller's reagent for 12 s to characterise the microstructure in the LPBF AlSi10Mg alloy via optical microscopy. Fig. 2 shows the microstructure of a top face and a side face with respect to the build process. The pores are "metallurgical" pores given their spherical geometry. The microstructure is consistent with that commonly reported in the literature [9], whereby α-Al columnar grains are surrounded by a continuous network of eutectic Si. This fine microstructure is made possible by the rapid cooling rates encountered during the LPBF process.

Each of the solid cylinders was machined into a tension test specimen according to the ASTM E8 standard, with a gauge section of length 30 mm and diameter 5 mm. Uniaxial tension tests were performed on the specimens in an INSTRON 5569 (INSTRON, MA, USA) electromechanical universal testing machine. An extensometer with a gauge length of 25 mm was used in conjunction with a 50 kN load cell. The crosshead speed was 0.45 mm min^{-1}, equivalent to a strain rate of 0.00025 s^{-1}. The extensometer directly recorded the strain data up to the point of fracture.

Fig. 3(a) shows the nominal stress–strain curves of LPBF AlSi10Mg alloys obtained from the tension tests. The Johnson–Cook constitutive

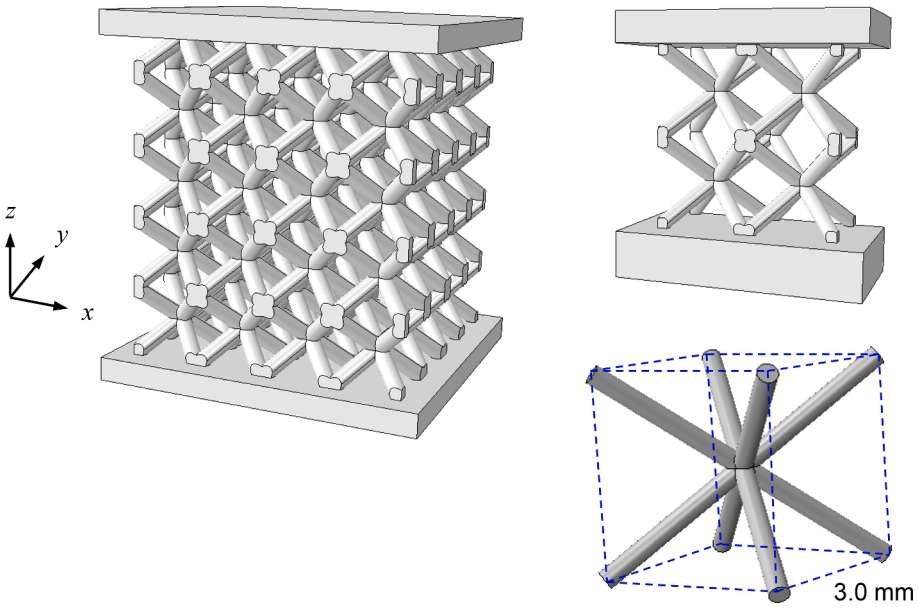

Fig. 1. Schematics of two configurations of large and small microlattice structures consisting of 4 × 4 × 4.5 and 2 × 1 × 2 body centred cubic (BCC) unit cells for uniaxial compression testing and a representative BCC unit cell in the microlattices.

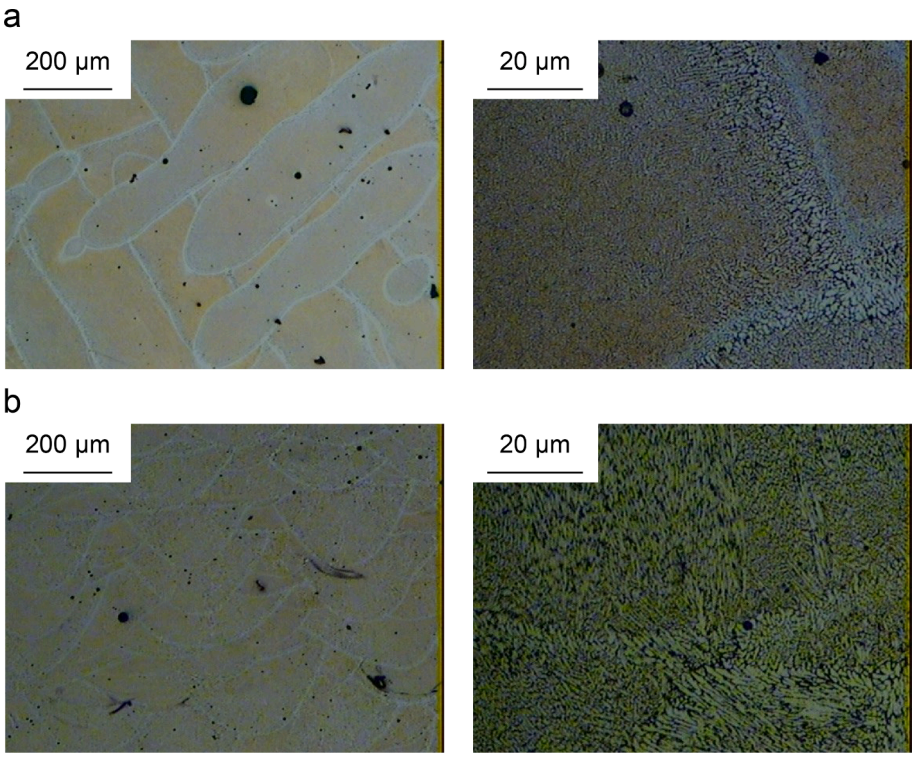

Fig. 2. Optical micrographs of microstructure on (a) the top face and (b) the side face of LPBF AlSi10Mg alloy specimens after etching.

hardening model was used to relate the true stress (σ) and true plastic strain ($\varepsilon_{\mathrm{pl}}$):

$$\sigma = A + B\,\varepsilon_{\mathrm{pl}}^{n} \tag{1}$$

where the material constants A = 231 MPa, B = 1030 MPa and n = 0.4711 were determined from the representative measured curve (Fig. 3 (b)). Ductile fracture with substantial dimples was observed on the fracture surface after the tension tests.

2.3. Uniaxial compression tests of large microlattices

Each of the large microlattice structures comprised 4 × 4 × 4.5 BCC unit cells after the EDM process (Fig. 1). Uniaxial compression tests on these specimens along the LPBF build direction were carried out in the same INSTRON machine affixed with a 5 kN load cell. Araldite Rapid epoxy adhesive was used to bond the top and bottom faces of each microlattice specimen to cylindrical solid 316L stainless steel blocks to prevent lateral sliding of the struts located there. The epoxy was cured overnight at room temperature and under pressure. A crosshead speed

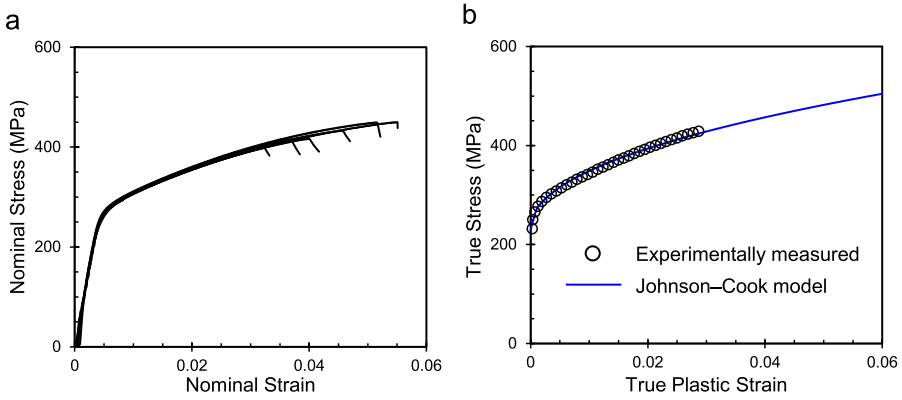

Fig. 3. (a) Nominal stress–strain curves of LPBF AlSi10Mg alloys measured in uniaxial tension tests and (b) the Johnson–Cook hardening model fitted from the measured stress–strain data.

corresponding to a strain rate of 0.001 s^{-1} was applied. This strain rate is of the same order of magnitude as the rate (0.00025 s^{-1}) in the uniaxial tension tests of bulk LPBF AlSi10Mg. Displacement (strain) measurements were obtained from the crosshead readings.

2.4. *In-situ SEM of uniaxial compression tests of small microlattices*

The configuration of small microlattices was designed to study the failure in struts and nodes via in-situ SEM of compression tests in a DEBEN 300N microtester (Fig. 4). As the load cell of the microtester has a force limit of 135 N, it was necessary to use a smaller number of unit cells for these microlattices. Uniaxial compression testing of large microlattices suggested that BCC microlattices with 2 × 1 × 2 unit cells were suitable for this particular experiment in terms of the peak force that these small microlattices with reduced cross section (two effective unit cells) can withstand (Fig. 1). These were obtained by sectioning the LPBF microlattices with 2 × 2 × 2 unit cells into half with a diamond wafering blade after they were separated from the substrate plate. The small microlattices had top and bottom end plates printed to laterally constrain them.

The microlattice specimens with 2 × 1 × 2 unit cells were tested in uniaxial compression at a displacement rate of 0.1 mm min^{-1} (equivalent to a strain rate of 0.00027 s^{-1}) along their build direction in the DEBEN microtester. The microtester was fully contained in the chamber of a JEOL (JEOL Ltd, Japan) JSM-5600LV SEM. Images were recorded on different regions of the observed side at various displacement stages of compression.

The main limitation of this experiment is that only the cracks on the side of each specimen facing the electron beam could be observed. Nevertheless, appropriate assumptions can be made on the state of the opposite side of each microlattice. As the microlattice is ideally symmetrical about the plane normal to the axis that bisects the microlattice, any cracks that can be observed on one side as per the experiment should ideally occur simultaneously on the opposite side, i.e. the rear side of the specimen.

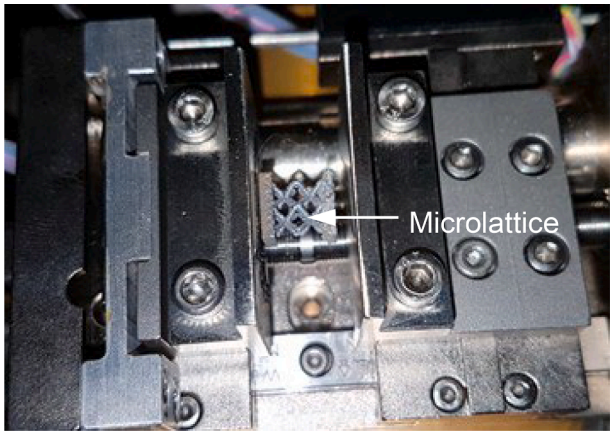

Fig. 4. In-situ SEM setup of uniaxial compression testing of a microlattice specimen with 2 × 1 × 2 unit cells in the DEBEN microtester.

3. Finite element modelling

Finite element modelling was performed in the ABAQUS (Dassault Systèmes Simulia Corp., RI, USA) software to study the deformation and localised stress field of the microlattice with 4 × 4 × 4.5 BCC unit cells subjected to quasi-static uniaxial compression. The geometrical model of the microlattice was generated using idealised struts. Although the use of imperfect struts would be a more accurate way to represent the microlattice under study, it greatly increases the computational time and the FE analysis may be unique to a single microlattice. So there exists a case for a more detailed investigation of the capability of FE models using idealised struts. Given the inherent difficulty in determining the effective diameter of LPBF struts, a parametric study was conducted to investigate the effect of the strut diameter on the stress–-strain response of microlattices. The diameters of random struts were measured with a digital calliper, and the variations were large with values typically between 500 and 600 μm. Based on the measured density of the bulk LPBF AlSi10Mg parent material and the microlattices, the average effective strut diameter of the microlattices was determined to be 527 μm, deviating from the nominal diameter 330 μm input for the LPBF process probably due to the larger melt pool for AlSi10Mg. Thus, three strut diameters d = 500, 600 and 700 μm were chosen in the parametric simulation. The unit cell edge length was L = 3.0 mm.

In the FE model, two plates were added to the top and bottom of the microlattice to constrain them laterally. Quadratic tetrahedral FE elements were used to mesh the microlattice and the plates. Note that a convergence study of the FE analysis was conducted to select the suitable element size. The constitutive model of LPBF AlSi10Mg was defined using the Johnson-Cook hardening equation (Eq. (1). The same boundary and loading conditions were applied to all the three parametric simulations. The bottom face of the bottom plate in each simulation was fixed while the top face of the top plate was loaded with a displacement equivalent to a nominal strain 0.1. A general interaction was introduced for all the surfaces whereby contact properties were defined with a penalty friction formulation (ballpark friction coefficient 0.1) for tangential behaviour and a “hard” contact for normal behaviour.

After the parametric simulations verified that the simulation with an idealised strut diameter of d = 500 μm agrees with the experimental

stress–strain curves prior to the peak stress (Section 4.1), the FE model was re-run on the microlattice with $d = 500$ μm with an extension of the final nominal strain up to 0.5. Finally, the FE model was re-run on a microlattice with 2 × 1 × 2 BCC unit cells and $d = 500$ μm to simulate the stress distribution under compression to a nominal strain 0.033 (displacement 0.2 mm) and further analyse the relation between crack initiation and localised stress.

Note that the standard implicit solver in ABAQUS was used in these simulations as no material damage model was incorporated. This is not to be confused with the subsequent simulations as explained in Section 4.5 that involve ductile damage models.

4. Results and discussion

4.1. Deformation behaviour of microlattices

The experimentally measured stress–strain curves of the large microlattice structures with 4 × 4 × 4.5 BCC unit cells are shown in Fig. 5. The curve shape is similar to that of many other cellular structures [1,10–12,32,33]. The overlapping curves for all the specimens up to their peaks indicate good reproducibility in the LPBF process and that the samples were cut consistently. Fig. 5 also illustrates the predicted curves of idealised microlattices with different strut diameters. The FE results of the microlattice with strut diameter $d = 500$ μm was found to almost coincide with the experimental stress–strain curves prior to the peak stress. This indicates an excellent agreement between the numerical predictions and experimental measurements. The input strut diameter of $d = 500$ μm in the FE simulation is close to the average effective diameter of 527 μm as measured experimentally. It appears that the averaging of the strut diameter allows for an accurate prediction of the overall stress–strain response of the microlattice in the elastic and plastic regimes prior to the peak stress.

The stress field and deformation process of the microlattices with $d = 500$ μm as predicted by the FE model are shown in Fig. 6. Beyond the strain corresponding to the experimental peak stress (Fig. 5), the predicted maximum von Mises stress in the microlattice can exceed the actual tensile strength of LPBF AlSi10Mg and continue increasing with the deformation (Fig. 6). This is because the yield stress extrapolated from the Johnson–Cook hardening model for AlSi10Mg increases with the plastic strain (Fig. 3(b)). Moreover, as no material damage model was incorporated in the FE simulation, the predicted curve starts to deviate away from the experimentally measured curves past the experimental peak stress (Fig. 5). This highlights the importance of incorporating an accurate damage model in FE simulations involving the failure of microlattices. In turn, the proper calibration and implementation of such a damage model is important. Nevertheless, the numerical results reported here without a damage model are valid for microlattices made of very ductile materials, e.g., LPBF stainless steel 316L [1].

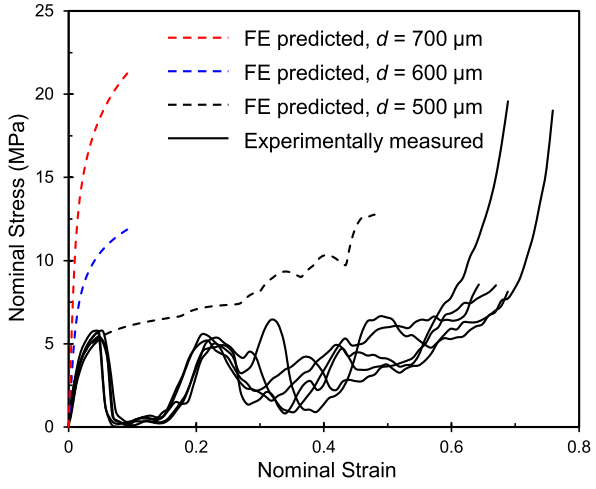

Fig. 5. Comparison between the FE predicted and experimentally measured stress–strain curves of the LPBF AlSi10Mg microlattice structures with 4 × 4 × 4.5 unit cells.

Different cross sections in the microlattice exhibit different nonuniform deformation patterns. Barrelling was observed, whereby the microlattice bulges outwards. Only the cross sections exactly halving the microlattice remain plane throughout the deformation process, while all other cross sections become more and more convex with respect to the midplanes of the microlattice (Fig. 6). Collectively, these cause a roughly X-shaped band of highly localised deformation to form gradually with the topmost and bottommost layers of unit cells deforming last. Based on the predictions on deformation alone (i.e., not considering material damage), it is likely that ultimately, within these competing planar bands, a crack will form in a strut first due to the geometrical imperfections introduced by the LPBF process, breaking the symmetry of the deformation and thus resulting in a diagonal shear band.

4.2. Failure mode in microlattices

The typical deformation and failure history of a tested large microlattice specimen is shown in Fig. 7. A diagonal shear band, although not predicted in the FE simulation with no material damage model, was observed in the experiments. Note that similar to the microlattice geometry, the predicted deformation pattern has two planes of symmetry, namely the planes perpendicular to the x and y axes (Fig. 6). However, the diagonal fracture pattern has only one plane of symmetry normal to either the x or y axis.

In the linear elastic and plastic regimes prior to the peak (from Fig. 7 (a) to (b)), deformation generally occurs throughout the entire microlattice. However, just beyond the peak stress (from Fig. 7(b) to (c)), two distinct segments can be discerned in the microlattice, which are separated by a plane running diagonally across the observed face. The diagonal plane would eventually form the shear band. Both the lower left and top right segments cease to deform any further, with the latter beginning to shear off along the diagonal plane. The deformation of the microlattice is localised within the diagonal shear band. The subsequent sharp drop in stress (from Fig. 7(c) to (d)) indicates the initiation or propagation of multiple cracks within the shear band (as detailed below), allowing the two segments to move more freely relative to each other in that direction.

4.3. Ductile fracture in microlattices

Similar localised failure processes were observed in all the tested small microlattices with 2 × 1 × 2 BCC unit cells under uniaxial compression. Fig. 8 shows a typical in-situ SEM observation of the failure phenomena at different displacement stages. The displacement readings would be overestimated for every point on their force–displacement curves, given that adhesive tape was used to secure the microlattice specimens to the compression platens in the microtester. Note that the peak force is close to but under the load cell capacity (135 N) of the DEBEN microtester, justifying the design of 2 × 1 × 2 unit cells in the small microlattices. The SEM images in Fig. 8 were produced from higher magnification images that were taken at various locations in the microlattice and then combined. The in-situ experiments provide evidence that cracks can initiate as early as just after the peak force is reached (Fig. 8(c)). The experiments suggest that the initiation and propagation of a crack can allow the small microlattice to maintain its current nominal stress level. The cracks were stable in that they did not propagate when compression was paused, and only did so with an increase in compressive displacement (Fig. 8(d) and (e)). The fracture surface of the final cracks exhibits substantial dimples (Fig. 9). Thus, the fracture in LPBF AlSi10Mg alloys is ductile in nature as also observed in

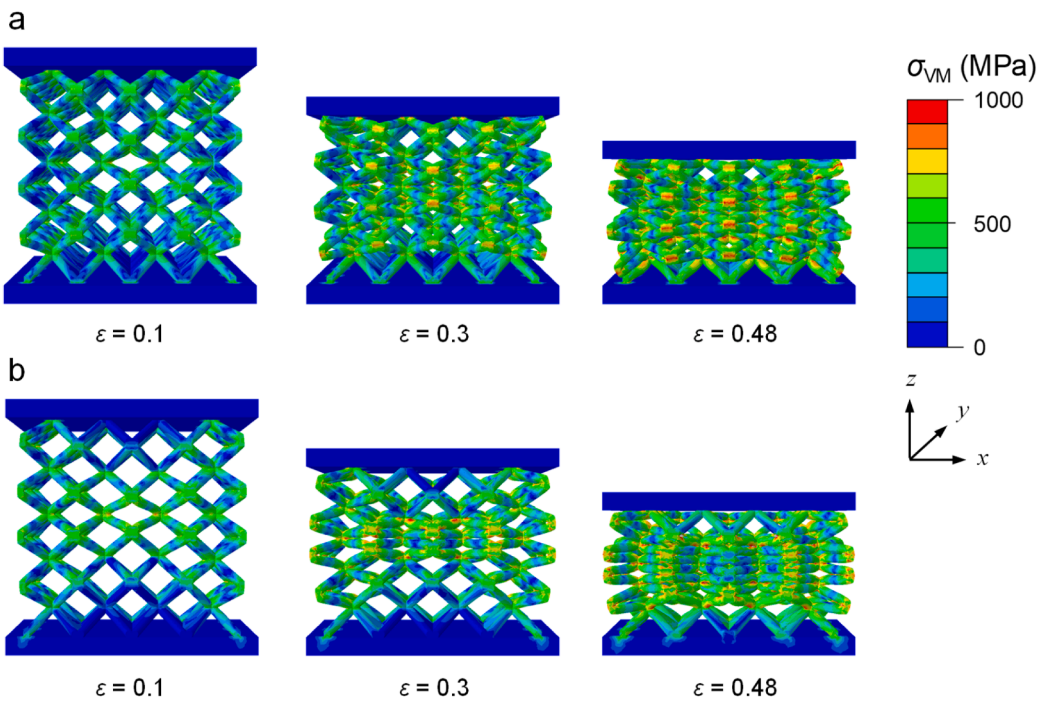

Fig. 6. Predicted von Mises stress distribution and deformation process in a microlattice structure with 4 × 4 × 4.5 unit cells at different strain stages of the uniaxial compression. (a) The free face of the entire microlattice and (b) the internal face on the rear half (two unit cell layers) are shown in the front view.

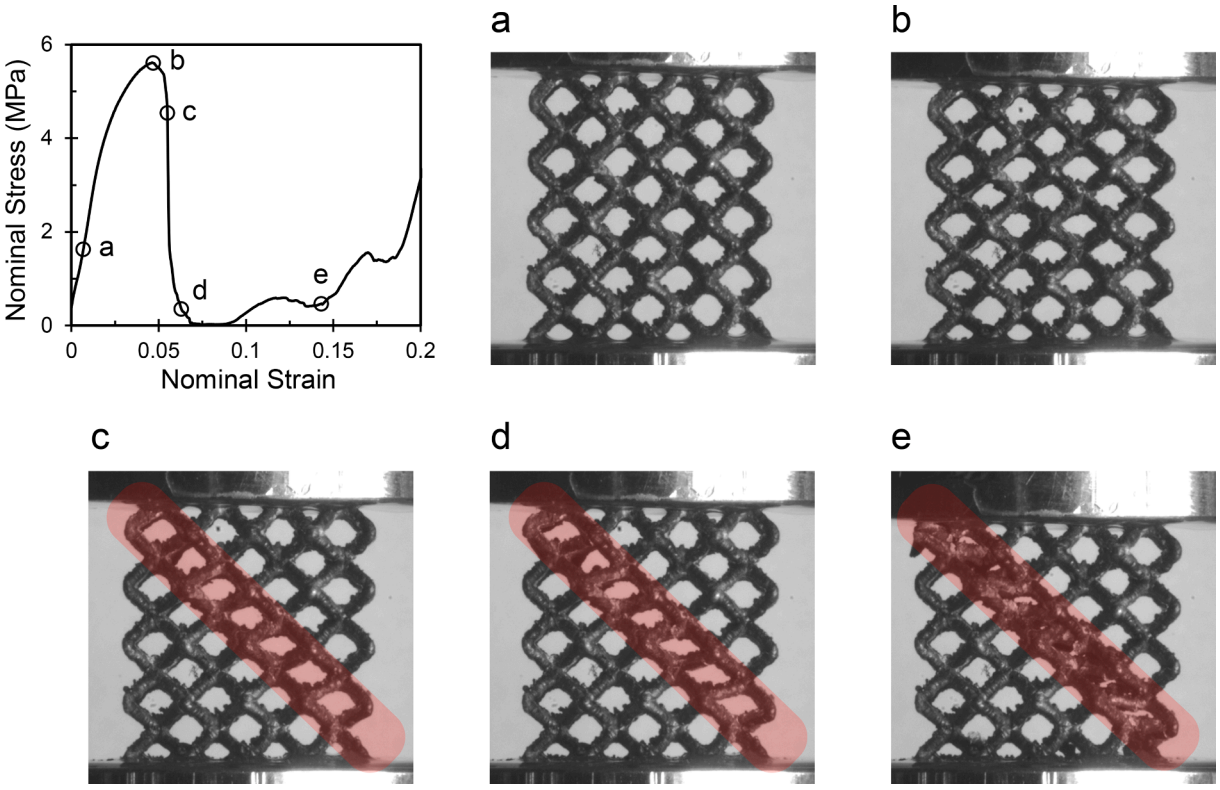

Fig. 7. Photography of the deformation history of a microlattice structure with 4 × 4 × 4.5 unit cells at five different strain stages (a to e) in the initial portion of the stress–strain curve under compression. The diagonal shear band is highlighted.

the fracture surface of bulk specimens subjected to uniaxial tension. Note that, for the case of large microlattices, it would be reasonable to expect that sharp drops after the peak stress are due to catastrophic failure with multiple cracks initiating or propagating simultaneously.

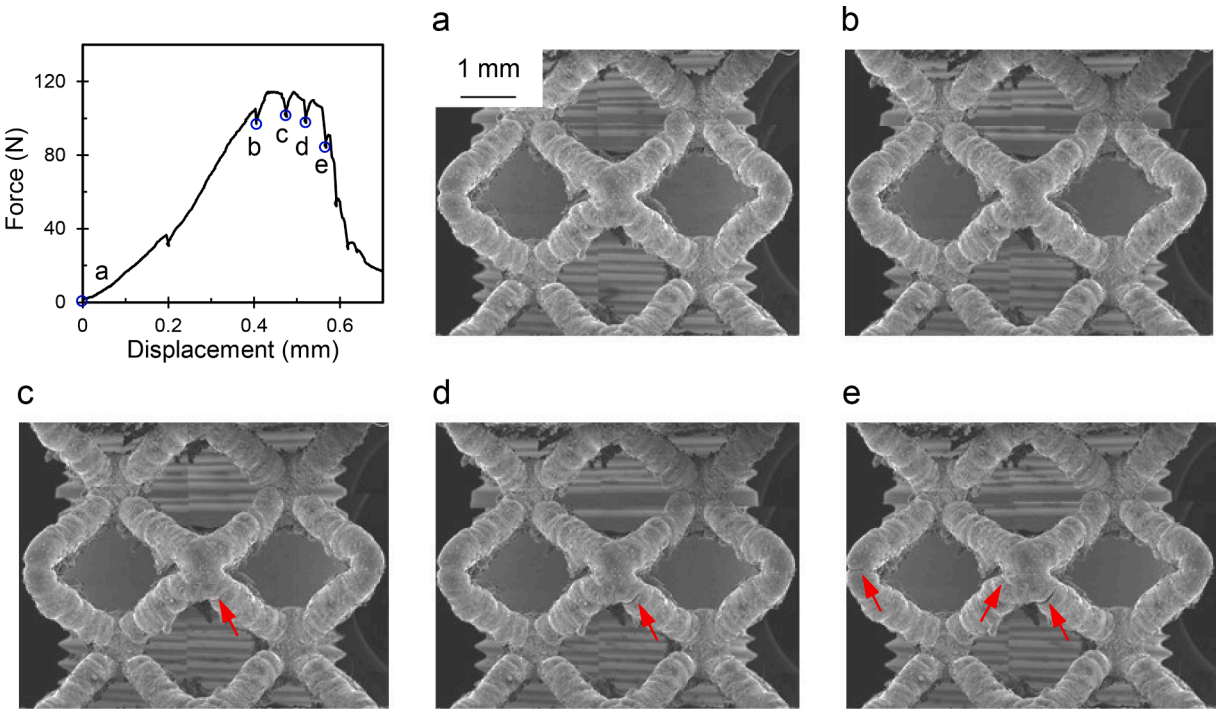

Fig. 8. SEM images of the deformation history of a microlattice structure with 2 × 1 × 2 unit cells at five different displacement stages (a to e) of the uniaxial compression in a microtester. Observed cracks are indicated by the arrows.

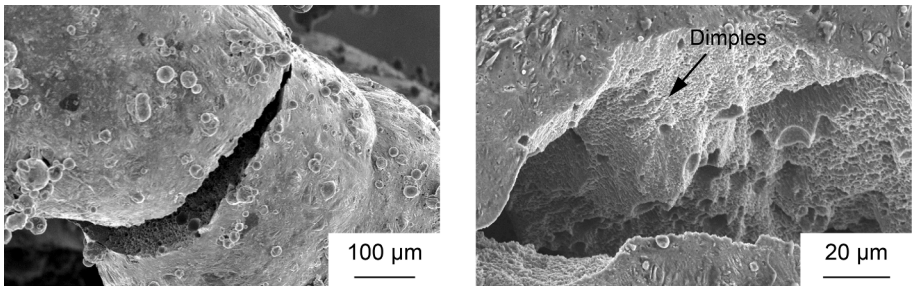

Fig. 9. A typical crack in microlattices and the fracture surface of a crack.

4.4. Relation between crack initiation and localised stress

On the observed face of each tested small microlattice specimen, the first crack always formed either right on the central node of the specimen or in its vicinity as shown in Fig. 8. The next cracks arose either at the left or the right node. The localised stress predicted by the FE simulation of the compression experiment of a small microlattice was then analysed and related to crack initiation.

4.4.1. Von Mises stress and equivalent plastic strain

Stress concentrates at the nodes as opposed to the struts in the microlattice. The eleven highlighted sites on each side (front and rear) of the microlattice experience the highest von Mises stress and equivalent plastic strain $\bar{\varepsilon}_{pl}$ levels (Fig. 10(a) and (b)). The middle of each strut can be ruled out as a potential crack initiation site given that it has not begun to yield at the global displacement in the simulation corresponding to that at which the specimens were observed to fail experimentally. However, this does not explain why the first crack forms only on or around site 6 when the other ten sites experience similar von Mises stress and equivalent plastic strain levels. While the initiation of a crack can be assumed to occur at a constant equivalent plastic strain, such a criterion does not take into account the stress triaxiality history over the entire loading process, which has been found to influence crack initiation in ductile fracture. Stress triaxiality is defined as hydrostatic stress divided by von Mises stress. Therefore, the maximum principal stresses at the eleven sites are discussed next, followed by their stress triaxialities.

4.4.2. Maximum principal stress and stress triaxiality

Within a laterally constrained microlattice, individual unit cells experience different boundary conditions. Different nodes undergo different stress levels depending on their relative positions within the microlattice (Fig. 10). It has been reported by Li [1] that internal nodes unaffected by microlattice edge effects experience compressive stresses on their lateral sides and tensile stresses on their top and bottom sides. However, this is not the case for those nodes exposed or near the top and bottom plates. Any of the nodes in the small microlattice is affected by edge effects, either being exposed or being located too close to the top or bottom plate as shown in Fig. 10. The exposed nodes experience tension on their outwards-facing lateral sides while on the nodes near the top or bottom plate there is some deviation from the reported stress state (Fig. 10(c)). These predictions are a direct consequence of the different boundary conditions experienced by the individual unit cells in the microlattice. Out of the eleven nodes experiencing high von Mises stress, only sites 5, 6 and 7 are in high tensile stress state (Fig. 10(c)).

A generic ductile fracture locus was used to make deductions that involved stress triaxiality. A fracture locus is a plot of equivalent plastic

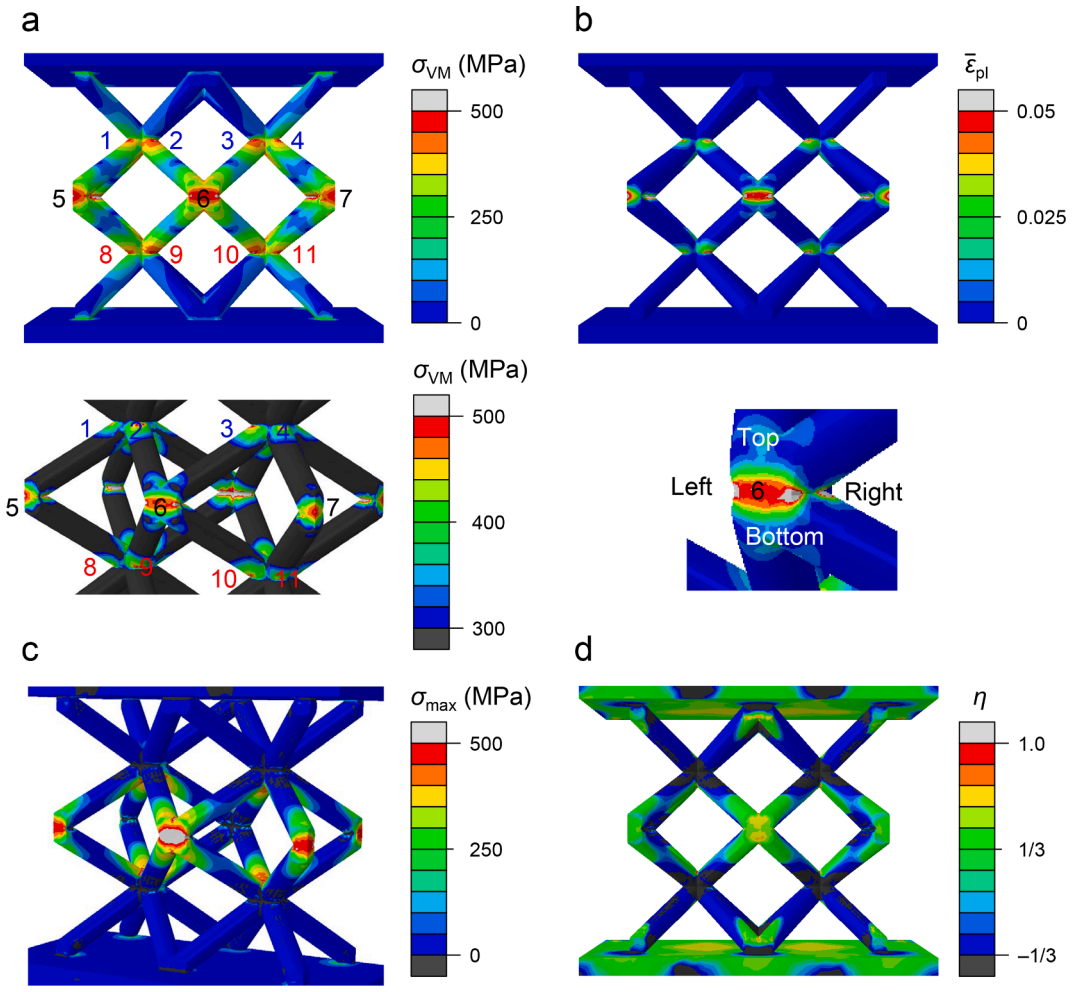

Fig. 10. Prediction of stress and strain states in a microlattice structure with 2 × 1 × 2 unit cells at the strain 0.033 (displacement 0.2 mm) of uniaxial compression: (a) von Mises stress, (b) equivalent plastic strain, (c) maximum principal stress and (d) stress triaxiality.

strain at fracture $\bar{\varepsilon}_{pl,\,f}$ versus stress triaxiality η. This generic fracture locus is defined for $\eta \geq -1/3$ and is monotonically decreasing. This assumed profile is similar to that of the Johnson-Cook damage model. The stress triaxiality histories of the eleven sites are plotted in Fig. 11. As

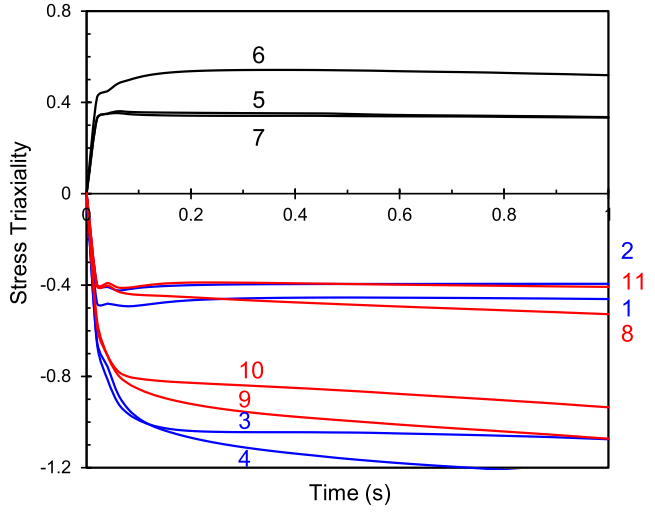

Fig. 11. Predicted stress triaxiality history of the eleven sites (as indicated in Fig. 10) of a microlattice structure with 2 × 1 × 2 unit cells.

they are relatively constant once the loading has begun, they can be assumed to be close to the average stress triaxiality values over the entire loading process. Since a crack can never initiate on a site at $\eta < -1/3$ regardless of how high the $\bar{\varepsilon}_{pl}$ is, sites 1 to 4 and 8 to 11 can be ruled out as potential crack initiation sites, leaving sites 5, 6 and 7 as the only possible ones (Fig. 10(d)).

4.4.3. *Crack initiation sites*

Site 6 (the central node) is unusual in that it was modelled as a planar surface in the idealised microlattice geometry (Fig. 10) to simply the analysis. The other ten sites were more localised, either being on shaper corners or on struts near nodes. A closer inspection of the $\bar{\varepsilon}_{pl}$ and η distributions reveals that for the idealised geometry, four points at the top, bottom, left, and right of site 6 should fracture first (Fig. 10(b) and (d)). For sites 5 and 7, while the η values are lower than that of site 6, the $\bar{\varepsilon}_{pl}$ are still very high. Since equivalent plastic strain at fracture $\bar{\varepsilon}_{pl,\,f}$ tends to decrease as stress triaxiality η increases past approximately $1/3$, it is possible for fracture to occur at a lower stress triaxiality as long as $\bar{\varepsilon}_{pl}$ exceeds $\bar{\varepsilon}_{pl,\,f}$. This is now in excellent agreement with the experimental observations: the first crack initiated at or around site 6 instead of other sites in the tested specimens and the next observed cracks around sites 5 and/or 7 (Figs. 8 and 10).

The locations of the first few cracks observed in a microlattice can deviate slightly from the predicted location in the idealised FE model due to imperfections in its struts and nodes. The first crack formed either on the central node (site 6) or near it, depending on the presence of

imperfections caused by the LPBF process in the forms of strut diameter variation and strut waviness [34], as well as their less than ideal surface finishing. These imperfections collectively prevent a planar surface from being achieved on the exposed nodes as should be the case for an idealised microlattice, instead resulting in rounded nodes. The imperfections also create regions of high stress concentration in the struts near these nodes, complicating the stress field around them. As shown in Fig. 8, the first crack on this tested microlattice initiated from a defect in the form of a contour. Thus, there is tendency for cracks to form on suitable defects where possible, i.e., near the regions of high stress concentration.

If a crack initiates away from the predicted location which is typically on a node, it will do so on a connecting strut near the node. This trend appears to hold true even for later cracks. The later cracks still initiated around these three sites (5, 6 and 7 in Fig. 8). This also suggests that the stress fields remained largely unchanged even after the first few cracks initiated.

Other than sites 5, 6 and 7 and their corresponding symmetric counterparts on the opposite face, only four other approximate sites within the entire small microlattice are potential crack initiation sites. These include the sites labelled A and B and the two sites under and facing sites A and B (Fig. 12). While they were expected to be unobservable as they were largely blocked from the electron beam in the SEM, crack initiation was fortunately captured in the in-situ SEM of compression tests of another small microlattice specimen (Fig. 12).

4.5. Prediction of failure in microlattices

The fracture strain ($\bar{\varepsilon}_{pl,\,f}$=0.03) of bulk LPBF AlSi10Mg in uniaxial tension testing (stress triaxiality $\eta = {}^{1}/_{3}$) as shown in Fig. 3(b) was used to estimate the fracture locus of the parent material (FL in Fig. 13). The fracture locus is similar to the Johnson–Cook damage criterion with a monotonically decreasing profile. In addition, based on the experimental results on aluminium alloy AA2024-T351 by Bao et al. [27,35], a cut off value of $\eta = -{}^{1}/_{3}$ is reasonable and was thus chosen for the estimated fracture locus. This was implemented in the form of a "vertical" asymptote (Fig. 13).

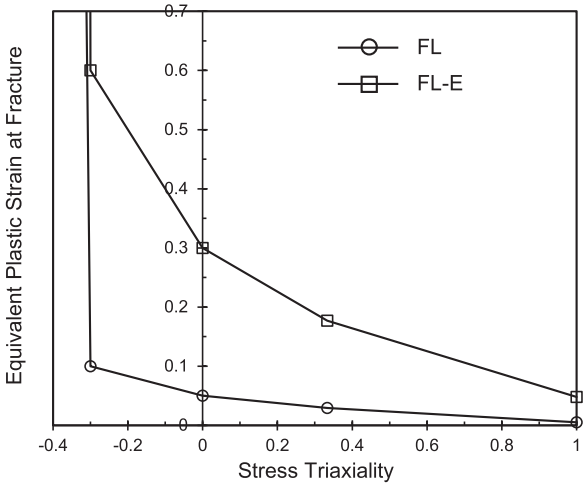

Fig. 13. Fracture locus (FL) of bulk LPBF AlSi10Mg estimated from uniaxial tension testing and effective fracture locus (FL-E) for the FE model that best fits the experimental results.

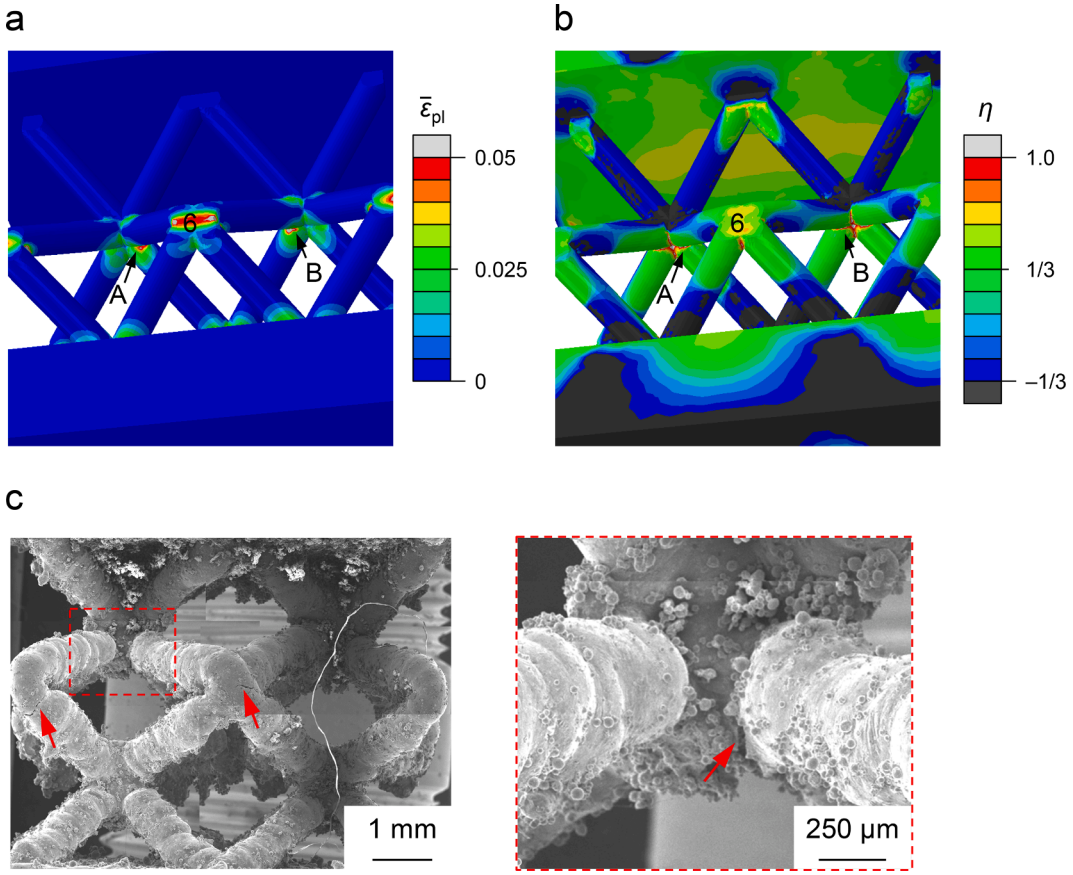

Fig. 12. Prediction of (a) equivalent plastic strain and (b) stress triaxiality in two internal sites within a microlattice structure with 2 × 1 × 2 unit cells at the strain 0.033 (displacement 0.2 mm) of uniaxial compression. (c) SEM image of another microlattice structure with 2 × 1 × 2 unit cells under uniaxial compression in the microtester.

The FE model of a large microlattice with 4 × 4 × 4.5 BCC unit cells and an idealised strut diameter $d = 500$ μm in compression was rerun with this fracture locus in ABAQUS. Note that the explicit solver was used this time as the deletion of finite elements based on the fracture locus was involved and cannot be easily handled by the standard implicit solver. The fracture locus data (FL in Fig. 13) was input to specify the ductile damage model in ABAQUS. It is almost impossible to have an unconstrained top plate in uniaxial compression experiments due to friction, as in the experiments on microlattices conducted in the present study. Furthermore, the actual microlattices most likely did not possess perfectly parallel top and bottom faces to which the anvils were glued, either due to the rough strut ends or less than ideal wire-cutting alignment, resulting in imperfect loading. In the FE model, it is therefore reasonable to impose a slight surface traction force parallel to the top face in one horizontal direction (the x direction in Fig. 14) and leave the displacement of the top plate free in that direction while locking the displacement in the other horizontal (y) direction. The imposed shear force (0.2 MPa) is only a small fraction of the peak compressive force (i.e., less than 4 % of about 6 MPa).

As shown in Fig. 14(a), the experimentally observed diagonal shear band was successfully predicted in the FE model of the large microlattice in compression. While the estimated monotonically decreasing fracture locus (FL) enabled the prediction of the correct failure mode, the predicted stress–strain curve departs significantly from the experimental curves (Fig. 15). As to why the FE model with this fracture locus underestimated the peak stress before failure, there are two likely reasons. Firstly, the local porosity at the crack initiation sites of the microlattice samples may be much lower than the average porosity in the uniaxial tension test samples. This is possible because these sites are much smaller than the uniaxial tension test samples, and thus may even be fully dense at these locations. Furthermore, the average porosity of microlattice struts may be lower than that of bulk material due to the LPBF process. This may imply that although the "stripes" scan strategy in LPBF is deemed more appropriate for fabricating larger size parts, it can also print small size features like struts in microlattices. Secondly, microlattice strut and node imperfections may result in more material being deposited at the crack initiation sites. In fact, this is the most likely reason why cracks sometimes initiate a small distance away from the numerically predicted sites.

In view of this, a reverse engineering approach was used to obtain the effective fracture locus (FL-E) for the FE model that best fits the experimental stress–strain curves (Fig. 15). Note that the effective fracture locus also assumes a monotonically decreasing profile. For FL-E, the equivalent plastic strain at fracture is about six times higher at $\eta = {}^1/_3$ than that determined by the uniaxial tension test (Fig. 13). The entire FL data was scaled up by a factor of approximately six to arrive at the FL-E in the reverse approach. Such a scale factor suggests that the postulated differences between bulk material and strut in terms of porosity and the geometrical deviations of the actual struts from ideal cylinders are deemed significant. The FE model with FL-E also successfully predicted the diagonal shear band as observed experimentally (Fig. 14(b)).

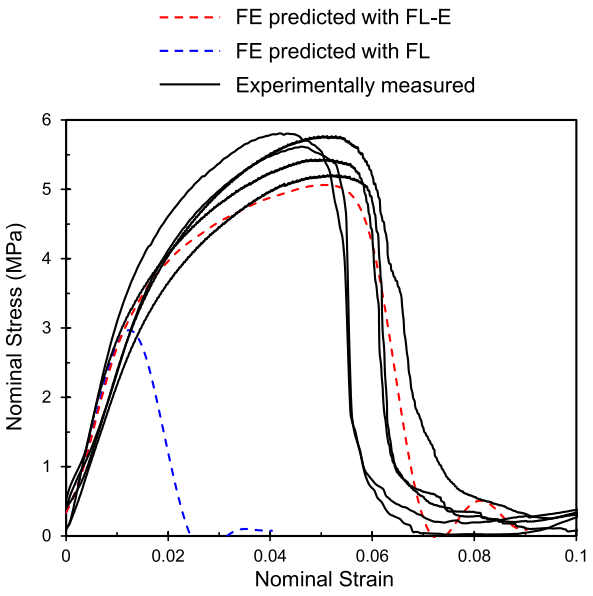

Fig. 15. Stress–strain curve of a microlattice with 4 × 4 × 4.5 unit cells in compression predicted by the FE model with two different fracture loci (FL and FL-E) and compared with the experimentally measured curves.

This FE simulation shows that in addition to localised deformation pattern and boundary conditions, the fracture locus profile significantly affects the stress–strain response and failure mode of the BCC microlattice structure.

5. Conclusions

Finite element modelling was developed to simulate the response of LPBF AlSi10Mg BCC microlattice structures in compression. An in-situ SEM observation of a BCC microlattice in uniaxial compression was combined with the FE simulation of this process to explore the fracture behaviour of microlattices. They provided insight into the spatial "resolution" of the numerical prediction of the sites of fracture when the actual sites of crack initiation are compared with the predicted ones. They also provided clues pertaining to the fracture locus of the parent material – bulk LPBF AlSi10Mg alloys. It was found that a crack initiation site must be in the suitably high equivalent plastic strain and stress triaxiality state based on the assumption that the parent material has a monotonically decreasing fracture locus, which was deemed

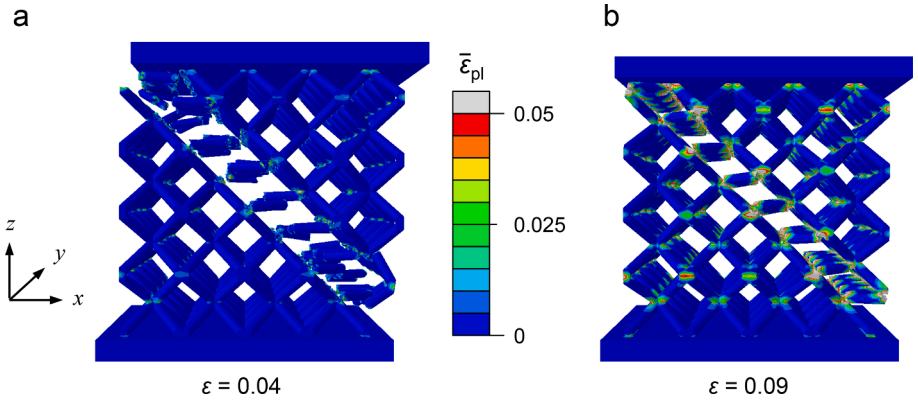

Fig. 14. Diagonal shear band in a microlattice structure with 4 × 4 × 4.5 unit cells in compression predicted by the FE model using (a) the estimated fracture locus (FL) and (b) the effective fracture locus (FL-E).

experimentally to be a reasonable one. Due to imperfections in struts and nodes, the actual locations of crack initiation may be shifted slightly from the sites predicted for a perfect microlattice. An assumed fracture locus and suitable boundary conditions were incorporated into the FE simulation and resulted in the successful prediction of the experimentally observed diagonal shear band. The effective fracture locus was obtained using a reverse approach so that the prediction best fits the experimental results. This work shows the importance of the parent material fracture locus in predicting crack initiation and propagation in microlattice structures and the failure modes of these structures.

Declaration of Competing Interest

The authors declare that they have no known competing financial interests or personal relationships that could have appeared to influence the work reported in this paper.

Data availability

Data will be made available on request.

Acknowledgements

This work was financially supported by the Medical Research Council (MRC) in the UK (MR/S010343/1) and Academic Research Fund Tier 1 by Ministry of Education, Singapore (RG72/20). NSKH acknowledges the Nanyang President's Graduate Scholarship which supported his PhD study at Nanyang Technological University and several research visits to University of Glasgow.

References

[1] P. Li, Constitutive and failure behaviour in selective laser melted stainless steel for microlattice structures, Mater. Sci. Eng. A 622 (2015) 114–120.
[2] O. Rehme, C. Emmelmann, Rapid Manufacturing of Lattice Structures with Selective Laser Melting. Laser-Based Micropackaging, 2006, 61070K.
[3] S. Van Bael, G. Kerckhofs, M. Moesen, G. Pyka, J. Schrooten, J.P. Kruth, Micro-CT-based improvement of geometrical and mechanical controllability of selective laser melted Ti6Al4V porous structures, Mater. Sci. Eng. A 528 (24) (2011) 7423–7431.
[4] B.B. Babamiri, B. Barnes, A. Soltani-Tehrani, N. Shamsaei, K. Hazeli, Designing additively manufactured lattice structures based on deformation mechanisms, Addit. Manuf. 46 (2021) 19.
[5] Y. Zhou, S. Shen, T. Liu, P. Li, F. Duan, Effective heat conduction evaluation of lattice structures from selective laser melting printing, Int. J. Heat Mass Transf. 218 (2024), 124790.
[6] X. Li, M. Zhao, X. Yu, J. Wei Chua, Y. Yang, K.M. Lim, W. Zhai, Multifunctional and customizable lattice structures for simultaneous sound insulation and structural applications, Mater. Des. 234 (2023), 112354.
[7] Q.X. Feng, Q. Tang, Z.M. Liu, Y. Liu, R. Setchi, An investigation of the mechanical properties of metallic lattice structures fabricated using selective laser melting, Proc. Inst. Mech. Eng. Pt. B-J. Eng. Manuf. 232 (10) (2018) 1719–1730.
[8] T.A. Schaedler, A.J. Jacobsen, A. Torrents, A.E. Sorensen, J. Lian, J.R. Greer, L. Valdevit, W.B. Carter, Ultralight Metallic Microlattices, Science 334 (6058) (2011) 962–965.
[9] M. Leary, M. Mazur, J. Elambasseril, M. McMillan, T. Chirent, Y.Y. Sun, M. Qian, M. Easton, M. Brandt, Selective laser melting (SLM) of AlSi12Mg lattice structures, Mater. Des. 98 (2016) 344–357.
[10] P. Li, Z. Wang, N. Petrinic, C.R. Siviour, Deformation behaviour of stainless steel microlattice structures by selective laser melting, Mater. Sci. Eng. A 614 (2014) 116–121.
[11] X. Shi, W. Liao, P. Li, C. Zhang, T. Liu, C. Wang, J. Wu, Comparison of Compression Performance and Energy Absorption of Lattice Structures Fabricated by Selective Laser Melting, Adv. Eng. Mater. 22 (11) (2020).
[12] Z. Wang, P. Li, Characterisation and constitutive model of tensile properties of selective laser melted Ti-6Al-4V struts for microlattice structures, Mater. Sci. Eng. A 725 (2018) 350–358.
[13] D.K. Do, P. Li, The effect of laser energy input on the microstructure, physical and mechanical properties of Ti-6Al-4V alloys by selective laser melting, Virtual Phys. Prototyp. 11 (1) (2016) 41–47.
[14] A. Leon, A. Shirizly, E. Aghion, Corrosion Behavior of AlSi10Mg Alloy Produced by Additive Manufacturing (AM) vs. Its Counterpart Gravity Cast Alloy, Metals 6 (7) (2016) 148.
[15] N.B. Ghisi, H. Ramos, L. Kindleyside, N.T. Aboulkhair, R. Santiago, The influence of the characteristic microstructure of additively manufactured AlSi10Mg on the plastic behaviour at various strain rates, Mater. Des. 223 (2022), 111112.
[16] K. Kempen, L. Thijs, J. Van Humbeeck, J.P. Kruth, Mechanical properties of AlSi10Mg produced by Selective Laser Melting, in: M. Schmidt, F. Vollertsen, M. Geiger (Eds.), Laser Assisted Net Shape Engineering 72012, pp. 439-446.
[17] M. Mazur, M. Leary, S.J. Sun, M. Vcelka, D. Shidid, M. Brandt, Deformation and failure behaviour of Ti-6Al-4V lattice structures manufactured by selective laser melting (SLM), Int. J. Adv. Manuf. Technol. 84 (5–8) (2016) 1391–1411.
[18] S. Drucker, M. Schulze, H. Ipsen, L. Bandegani, H. Hoch, M. Kluge, B. Fiedler, Experimental and numerical mechanical characterization of additively manufactured Ti6Al4V lattice structures considering progressive damage, Int. J. Mech. Sci. 189 (2021) 12.
[19] R. Chen, S. Wang, Z. Wu, Y. Jia, W. Zhang, B. Cao, X. Song, Q. Ma, C. Li, J. Du, S. Yu, J. Wei, Compressive enhancement gyroid lattice with implicit modeling implementation and modified G-A model property prediction, Mater. Des. 232 (2023), 112153.
[20] X. Cai, C. Pan, J. Wang, W. Zhang, Z. Fan, Y. Gao, P. Xu, H. Sun, J. Li, W. Yang, Mechanical behavior, damage mode and mechanism of AlSi10Mg porous structure manufactured by selective laser melting, J. Alloys Compd. 897 (2022), 162933.
[21] K. Ushijima, W.J. Cantwell, R.A.W. Mines, S. Tsopanos, M. Smith, An investigation into the compressive properties of stainless steel micro-lattice structures, J. Sandw. Struct. Mater. 13 (3) (2011) 303–329.
[22] O. Cansizoglu, O. Harrysson, D. Cormier, H. West, T. Mahale, Properties of Ti-6Al-4V non-stochastic lattice structures fabricated via electron beam melting, Mater. Sci. Eng. A 492 (1–2) (2008) 468–474.
[23] S. Tsopanos, R.A.W. Mines, S. McKown, Y. Shen, W.J. Cantwell, W. Brooks, C. J. Sutcliffe, The Influence of Processing Parameters on the Mechanical Properties of Selectively Laser Melted Stainless Steel Microlattice Structures, J. Manuf. Sci. Eng. – Trans. ASME 132 (4) (2010).
[24] R. Mahshid, H.N. Hansen, K.L. Hojbjerre, Strength analysis and modeling of cellular lattice structures manufactured using selective laser melting for tooling applications, Mater. Des. 104 (2016) 276–283.
[25] G.N. Labeas, M.M. Sunaric, Investigation on the Static Response and Failure Process of Metallic Open Lattice Cellular Structures, Strain 46 (2010) 195–204.
[26] M. Smith, Z. Guan, W.J. Cantwell, Finite element modelling of the compressive response of lattice structures manufactured using the selective laser melting technique, Int. J. Mech. Sci. 67 (2013) 28–41.
[27] Y.B. Bao, T. Wierzbicki, On fracture locus in the equivalent strain and stress triaxiality space, Int. J. Mech. Sci. 46 (1) (2004) 81–98.
[28] T. Wierzbicki, Y.B. Bao, Y.W. Lee, Y.L. Bai, Calibration and evaluation of seven fracture models, Int. J. Mech. Sci. 47 (4–5) (2005) 719–743.
[29] J. Kadkhodapour, H. Montazerian, A.C. Darabi, A.P. Anaraki, S.M. Ahmadi, A. A. Zadpoor, S. Schmauder, Failure mechanisms of additively manufactured porous biomaterials: Effects of porosity and type of unit cell, J. Mech. Behav. Biomed. Mater. 50 (2015) 180–191.
[30] F. Concli, A. Gilioli, Numerical and experimental assessment of the mechanical properties of 3D printed 18-Ni300 steel trabecular structures produced by Selective Laser Melting - a lean design approach, Virtual Phys. Prototyp. 14 (3) (2019) 267–276.
[31] N.T. Aboulkhair, I. Maskery, C. Tuck, I. Ashcroft, N.M. Everitt, The microstructure and mechanical properties of selectively laser melted AlSi10Mg: The effect of a conventional T6-like heat treatment, Mater. Sci. Eng. A 667 (2016) 139–146.
[32] N.S.K. Ho, P. Li, S. Raghavan, T. Li, The effect of slurry composition on the microstructure and mechanical properties of open-cell Inconel foams manufactured by the slurry coating technique, Mater. Sci. Eng. A 687 (2017) 123–130.
[33] P. Li, N. Ngoc Vu, H. Hao, Dynamic compressive behaviour of Mg foams manufactured by the direct foaming process, Mater. Des. 89 (2016) 636–641.
[34] L. Liu, P. Kamm, F. Garcia-Moreno, J. Banhart, D. Pasini, Elastic and failure response of imperfect three-dimensional metallic lattices: the role of geometric defects induced by Selective Laser Melting, J. Mech. Phys. Solids 107 (2017) 160–184.
[35] Y.B. Bao, T. Wierzbicki, On the cut-off value of negative triaxiality for fracture, Eng. Fract. Mech. 72 (7) (2005) 1049–1069.